

## Transformation of polar nematic phases in the presence of an electric field

A. V. Emelyanenko <sup>1,\*</sup>, V. Yu. Rudyak <sup>1</sup>, S. A. Shvetsov<sup>1</sup>, F. Araoka <sup>2</sup>, H. Nishikawa<sup>2</sup> and K. Ishikawa <sup>3</sup>

<sup>1</sup>*Lomonosov Moscow State University, Moscow 119991, Russia*

<sup>2</sup>*RIKEN Center for Emergent Matter Science (CEMS), 2-1 Hirosawa Wako, Saitama 351-0198, Japan*

<sup>3</sup>*Tokyo Institute of Technology, 2-12-1 Ookayama, Meguro-ku, Tokyo 152-8550, Japan*



(Received 30 July 2023; accepted 7 December 2023; published 18 January 2024)

Only a few years have passed since the discovery of polar nematics, and now they are becoming the most actively studied liquid-crystal materials. Despite numerous breakthrough findings made recently, a theoretical systematization is still lacking. In the present paper, we take a step toward systematization. The powerful technique of molecular-statistical physics has been applied to an assembly of polar molecules influenced by electric field. Three polar nematic phases were found to be stable at various conditions: the double-splay ferroelectric nematic  $N_F^{2D}$  (observed in the lower-temperature range in the absence of or at low electric field), the double-splay antiferroelectric nematic  $N_{AF}$  (observed at intermediate temperature in the absence of or at low electric field), and the single-splay ferroelectric nematic  $N_F^{1D}$  (observed at moderate electric field at any temperature below transition into paraelectric nematic  $N$  and in the higher-temperature range (also below  $N$ ) at low electric field or without it. A paradoxical transition from  $N_F^{1D}$  to  $N$  induced by application of higher electric field has been found and explained. A transformation of the structure of polar nematic phases at the application of electric field has also been investigated by Monte Carlo simulations and experimentally by observation of polarizing optical microscope images. In particular, it has been realized that, at planar anchoring,  $N_{AF}$  in the presence of a moderate out-of-plane electric field exhibits twofold splay modulation: antiferroelectric in the plane of the substrate and ferroelectric in the plane normal to the substrate. Several additional subtransitions related to fitting the confined geometry of the cell by the structure of polar phases were detected.

DOI: [10.1103/PhysRevE.109.014701](https://doi.org/10.1103/PhysRevE.109.014701)

### I. INTRODUCTION

One of the main trends in modern science today is the development of new materials, which can be effectively manipulated by electric field for various human needs, from displays to medicine. Liquid crystals (LCs) fulfill many demands. It was noticed that LCs possessing spontaneous polarization can be better candidates for novel applications: from fast energy-saving and compact electronics to artificial muscles. However, the layered structures of smectics (the only class of LCs known previously to possess spontaneous polarization) are poorly resistant to mechanical stress. Over the past few years, several new classes of nematic LCs (which are sustainable to mechanical stress) with unique properties originating from the unique symmetry of individual molecules have been discovered.

For the past few decades, the formation of spontaneous polarization in nematic materials has been actively discussed [1–4]. Liquid crystals consisting of bent-core molecules were considered as the main candidates, since they have a significantly (several orders of magnitude) higher flexoelectric coefficient [5]. Indeed, nanosized polar clusters in the nematic phase were found for this and other kinds of mesogens [6,7]. However, these materials do not possess macroscopic polarization in the absence of external field. Meanwhile, proper ferroelectricity was found in columnar phases composed of

umbrella-shaped mesogens [8–10] and in reentrant smectic phases [11–15].

In 2017, the two scientific groups independently reported on the existence of polar nematic phases in LCs composed of wedge-shaped molecules [16–18]. In Refs. [19,20] it was realized that the polar nematic phases can demonstrate spontaneous splay and flexoelectricity, while the existence of splay flexoelectricity in nematic LCs was predicted earlier theoretically in Ref. [21]. It was also noticed in Refs. [22–26] that minor changes in the molecular shape can sufficiently modify the phase sequence.

In Ref. [16] it was demonstrated that DIO material possesses at least three nematic phases: a conventional paraelectric nematic phase ( $N$  or  $M1$ ) at higher temperature, a ferroelectric nematic phase ( $N_F$  or  $MP$ ) at lower temperature, and some intermediate phase ( $N_X$  or  $M2$ ) in between them.  $M2$  is also reported as  $\text{SmZ}_A$  phase in Ref. [27], where the evidence of translational correlations of DIO molecules is presented. In Refs. [17,18] and later in Ref. [28] it was confirmed that RM-734 material demonstrates  $N_F$ , but does not demonstrate  $N_X$ . The anomalously high dielectric permittivity and dielectric anisotropy were found in the  $N_F$  phase in both DIO and RM-734 materials [29]. The value of spontaneous polarization in  $N_F$  is comparable with that for the solid-state ferroelectrics [30]. At present, many other polar nematic (including chiral and biaxial) phases were found in different materials and mixtures [31–34]. Our theoretical studies presented in Ref. [35] suggest that the intermediate  $M2$  (or  $N_X$ ) phase observed in DIO can be the antiferroelectric double splay nematic phase (in correspondence with the

\*emel@polly.phys.msu.ru

definition and in complete agreement with Refs. [36,37]) forming the periodic 2D-splay domains of several micrometers size. The same conclusions follow from dielectric measurements and polarizing optical microscope (POM) observations in Refs. [16,38], measurements of spontaneous polarization and piezoresponse force microscopy observations in Ref. [28], and dielectric spectroscopy measurements [39].

Experimentally, it is becoming more and more evident [40] that ferroelectric nematic phase ( $MP$  or  $N_F$ ) also possesses the splay domains. For the uniformity of description, here and below we are going to use the  $N_F^{1D}$  and  $N_F^{2D}$  notations by combining “ $N_F$ ” with “single-splay” or “double-splay” definitions introduced in Refs. [36,37]). To be consistent, furthermore, we are going to use the  $N_{AF}$  notation for  $M2$  ( $N_X$ ), which is antiferroelectric.

There are many expectations about applications of nematic ferroelectrics (NFs). Generally, their behavior at application of electric field is not trivial, particularly in combination with electric field and surface-related effects [41,42]. NFs are good candidates in nonlinear optics [43]. Interesting effects related to the motion of ferroelectric nematic droplets in isotropic melts are considered in Ref. [44], the light-induced branched structures of NF droplets on the surfaces are observed in Ref. [45], and the optically controlled motion of NF droplets on a ferroelectric substrate was observed in Ref. [46]. Various polarization topologies in confined NFs were discussed in Ref. [47]. Recently, the behavior of ferroelectric nematics confined in microchannels under action of electric field was investigated in Ref. [48].

The discussion on how many polar nematic phases can exist, which of them are splayed and which are uniform, which of them are proper and which are improper, is ongoing. Recently, Ref. [49] reported the existence of three kinds of NF phases. In the present paper, we justify the existence of three (macroscopically uniaxial and achiral) polar nematic phases. In particular, we expect that all three polar phases can be observed in DIO material. We are going to present theoretical explanations for why all three polar phases are splayed and improper ferroelectric. At the same time, since the splay domain size can achieve several micrometers in some temperature ranges, the splay director deformation can be suppressed by the surfaces if the cell thickness is lower than the domain size.

The paper is organized as follows. In Sec. II the structures of polar nematic phases merged from theory, computer simulations, and experiment will be outlined and systemized. In Sec. III the transformations of polar nematic phases induced by variation of temperature and electric field will be investigated. In Sec. IV the theoretical approaches used for analysis of the structures of polar nematic phases will be presented. Finally, in Sec. V the conclusions will be made.

## II. THE STRUCTURES OF POLAR NEMATIC PHASES MERGED FROM THEORY, COMPUTER SIMULATIONS, AND EXPERIMENT

### A. Generalization of elastic free energy for the presence of flexoelectric and induced polarizations

It is known that the flexoelectric effect is crucial for the formation of various polar nematic phases. We are considering

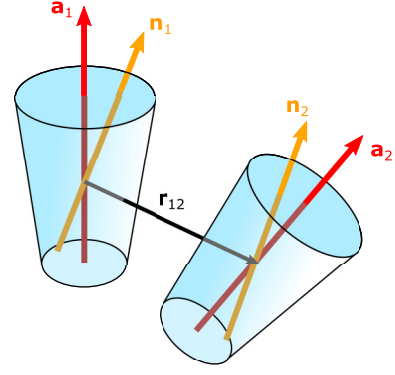


FIG. 1. A pair of interacting polar molecules. Adapted from Ref. [35].

polar molecules similarly to that presented in Ref. [35]. Technically, the flexoelectric term in the free energy can be obtained from consideration of specific symmetry of the pair molecular potential. In particular, the effective pair molecular interaction potential  $U_{12}^{ef}(\mathbf{a}_1, \mathbf{a}_2, \mathbf{r}_{12})$  can be approximated by spherical invariants  $T_{\ell L \lambda}(\mathbf{a}_1, \mathbf{u}_{12}, \mathbf{a}_2)$ , where  $\mathbf{a}_1$  and  $\mathbf{a}_2$  are the principal axes of molecules 1 and 2 located at points  $\mathbf{r}_1$  and  $\mathbf{r}_2$ , respectively, and  $\mathbf{u}_{12} \equiv \mathbf{r}_{12}/|\mathbf{r}_{12}|$  is the unit intermolecular vector,  $\mathbf{r}_{12} \equiv \mathbf{r}_2 - \mathbf{r}_1$  (Fig. 1):

$$U_{12}^{ef}(\mathbf{a}_1, \mathbf{a}_2, \mathbf{r}_{12}) = - \sum_{\ell, L, \lambda} J_{\ell L \lambda}(r_{12}) T_{\ell L \lambda}(\mathbf{a}_1, \mathbf{u}_{12}, \mathbf{a}_2). \quad (1)$$

Introducing the polar  $P(\mathbf{r})$  and nonpolar  $S(\mathbf{r})$  orientational order parameters

$$P(\mathbf{r}) \equiv \int f[(\mathbf{a} \cdot \mathbf{n}), \mathbf{r}] P_1(\mathbf{a} \cdot \mathbf{n}) d^2 \mathbf{a},$$

$$S(\mathbf{r}) \equiv \int f[(\mathbf{a} \cdot \mathbf{n}), \mathbf{r}] P_2(\mathbf{a} \cdot \mathbf{n}) d^2 \mathbf{a}, \quad (2)$$

where  $P_1$  and  $P_2$  are the first and second Legendre polynomials, and  $f[(\mathbf{a} \cdot \mathbf{n}), \mathbf{r}]$  is the orientational distribution function for molecules having principal axes  $\mathbf{a}$  with respect to director  $\mathbf{n}$  at point  $\mathbf{r}$ , and using the gradient expansion of the director [50,51], we obtain the flexoelectric term as the average of  $T_{110}(\mathbf{a}_1, \mathbf{u}_{12}, \mathbf{a}_2)$  and  $T_{011}(\mathbf{a}_1, \mathbf{u}_{12}, \mathbf{a}_2)$  polar invariants [35]:

$$(J_{110}(r_{12}) T_{110}(\mathbf{a}_1, \mathbf{u}_{12}, \mathbf{a}_2) + J_{011}(r_{12}) T_{011}(\mathbf{a}_1, \mathbf{u}_{12}, \mathbf{a}_2)) \implies \lambda P(\nabla \cdot \mathbf{n}), \quad (3)$$

where  $\lambda$  is proportional to the flexoelectric coefficient. The elastic free-energy density can be generalized by inclusion of the flexoelectric splay term and the term related to the presence of external electric field:

$$\frac{\partial F_n}{\partial V} = \frac{1}{2} K_{11} \{ \mathbf{n}(\nabla \cdot \mathbf{n}) - \lambda \mathbf{P} \}^2 + \frac{1}{2} K_{22} (\mathbf{n} \cdot [\nabla \times \mathbf{n}])^2 + \frac{1}{2} K_{33} [\mathbf{n} \times [\nabla \times \mathbf{n}]]^2 - \varepsilon_a (\mathbf{E} \cdot \mathbf{P}), \quad (4)$$

where  $\mathbf{P}(\mathbf{r})$  is the vector having absolute value  $P(\mathbf{r})$  [see the definition in Eq. (2)] and (at positive  $P$ ) parallel to a particular direction (one of the two opposite directions) of pseudovector  $\mathbf{n}(\mathbf{r})$ ;  $K_{11}$ ,  $K_{22}$ , and  $K_{33}$  are the splay, twist, and bend elastic constants, respectively;  $K_{11} \lambda$  is the flexoelectric constant

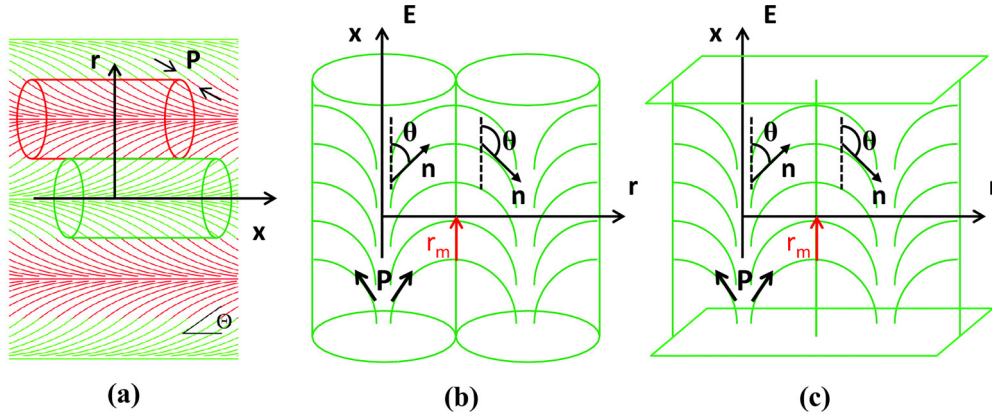


FIG. 2. Director distribution in  $N_{AF}$  (a),  $N_F^{2D}$  (b), and  $N_F^{1D}$  (c). Green corresponds to the positive splay and polarization, red corresponds to the negative splay and polarization; the  $\mathbf{x}$ -axis is either along the domain symmetry axis in (a) and (b) or along the symmetry plane in (c); the  $\mathbf{r}$ -axis is perpendicular to the  $\mathbf{x}$ -axis;  $\theta$  is the angle between the local director  $\mathbf{n}$  and the  $\mathbf{x}$ -axis;  $\mathbf{P}$  is the local polarization.

[Eq. (3)]; and  $\varepsilon_a$  is the dielectric anisotropy of the material. At positive  $\lambda$ , polarization  $\mathbf{P}$  is parallel to director  $\mathbf{n}$  at positive splay ( $\nabla \cdot \mathbf{n}$ ), and it is antiparallel to  $\mathbf{n}$  at negative splay. Here we should note that Eq. (4) is only a part of the free-energy density, which explicitly depends on director  $\mathbf{n}$ , but it does not contain all the terms depending on the polarization value  $P$ . The total free-energy density will be considered in Sec. IV.

### B. Equilibrium structures of polar nematic phases

To obtain the equilibrium structures of polar nematic material at various conditions, we should minimize the total free energy independently with respect to director  $\mathbf{n}(\mathbf{r})$  and orientational distribution function  $f[(\mathbf{a} \cdot \mathbf{n}), \mathbf{r}]$ . The whole director-dependent part of the free-energy density is presented in Eq. (4), while the total free-energy density depending explicitly on the orientational distribution function  $f[(\mathbf{a} \cdot \mathbf{n}), \mathbf{r}]$  will be considered in the framework of molecular statistical theory in Sec. IV A. One notes, however, that Eq. (4) contains also polarization  $\mathbf{P}(\mathbf{r})$ , which is determined by the function  $f[(\mathbf{a} \cdot \mathbf{n}), \mathbf{r}]$  in correspondence with Eq. (2), and therefore the director and the orientational distribution function are correlated. This correlation will be considered in the framework of perturbation theory in Sec. IV B. The theoretical part requires, however, some geometrical simplification, such as consideration of the axial and planar symmetries. Within these symmetry restrictions, at various conditions we find the three basic structures, which are presented in Fig. 2. At the same time, from computer simulations (Sec. IV C) we can see the more detailed information about the transformations between structures presented in Fig. 2, and the transient structures have obviously more complex geometry. The first basic structure is the double-splay antiferroelectric nematic phase  $N_{AF}$  (designated also  $N_X$  or  $M2$  elsewhere) with alternating signs of the splay and polarization in space. The other two basic structures, stable at different conditions, are the double- and single-splay ferroelectric nematics,  $N_F^{2D}$  and  $N_F^{1D}$ , respectively.  $N_F^{2D}$  and  $N_{AF}$  are composed of quasicylindrical periodic domains, while  $N_F^{1D}$  is composed of planar periodic domains. For each structure presented in Fig. 2, the  $\mathbf{x}$ -axis can be introduced, to which the director is parallel in the middle of each domain. In  $N_F^{2D}$  and  $N_{AF}$ , the director exhibits variation along radius  $\mathbf{r}$  of the

cylinder, while in  $N_F^{1D}$  the director exhibits variation along the single space direction (for uniformity of equations, also designated as  $\mathbf{r}$ ). In all cases,  $\mathbf{r}$  is perpendicular to  $\mathbf{x}$ . In ferroelectric phases,  $N_F^{2D}$  and  $N_F^{1D}$ , the projection of polarization on the  $\mathbf{x}$ -axis does not alternate in sign, while in antiferroelectric  $N_{AF}$ , polarization alternates periodically in sign along each Cartesian coordinate.

The electric field–temperature phase diagram is presented in Fig. 3(a), while the temperature dependencies of the domain radius and characteristic polar order parameter at  $E = 0$  are presented in Figs. 3(b) and 3(c), respectively. From theory (Sec. IV B) it follows that, within each polar phase, the domain radius  $r_m$  increases and polarization  $P^*$  decreases with increasing temperature, while multiple  $r_m P^*$  remains constant. At zero electric field,  $N_F^{2D}$  minimizes the free energy at lower temperature,  $N_F^{1D}$  phase minimizes the free energy at higher temperature, and  $N_{AF}$  minimizes the free energy in between. The domains in  $N_F^{2D}$  and  $N_{AF}$  are visible with a microscope [see Figs. 4(a) and 4(b), respectively]; their typical size is several micrometers. In the absence of an electric field, the domains in  $N_F^{1D}$  at planar anchoring [Fig. 4(c)] are not visible, because the energy-optimal configuration of the domains makes no optical difference between any points on the glass substrate. In the absence of electric field, the antiferroelectric single-splay phase [Fig. 4(d)] possesses the same free energy as the ferroelectric one. The plane of each arc in Figs. 4(c) and 4(d) can be vertical or tilted. At moderate values of electric field, all the splay nematic phases transform into  $N_F^{1D}$  [the orientations of arcs in  $N_F^{1D}$  in the presence of moderate electric field are shown in Fig. 4(e), they can be vertical ( $\beta = 0$ ) or tilted ( $\beta \neq 0$ ) to fit the cell gap] and at higher values of electric field—into paraelectric  $N$  having uniform director orientation.

## III. TRANSFORMATIONS OF POLAR NEMATIC PHASES INDUCED BY VARIATION OF TEMPERATURE AND ELECTRIC FIELD

### A. Transformation of $N_{AF}$ and $N_F^{2D}$ into $N_F^{1D}$ in electric field

Let us consider the variation of  $N_{AF}$  in the electric field, as it seen from POM and computer simulations (Sec. IV C).

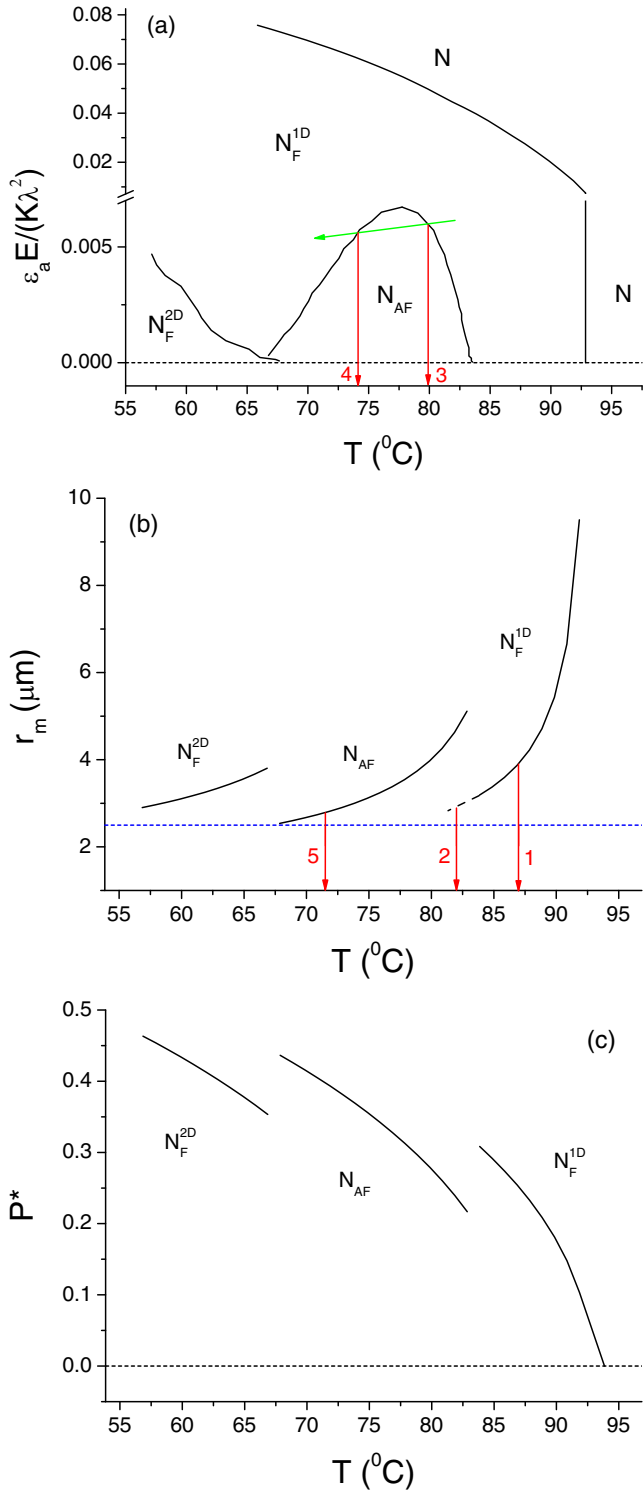


FIG. 3. Electric field–temperature phase diagram (a); Temperature dependencies of the domain radius (b) and characteristic polar order parameter (c) at  $E = 0$ . Green arrow in (a) tentatively corresponds to the phase sequence with temperature variation at fixed  $E \neq 0$ . Red arrows with numbers in (a) and (b) correspond to the temperatures of specific phase transitions observed experimentally (Sec. III B). Dashed blue line in (b) corresponds to the half-thickness of the cell. Molecular parameters are the same as in the caption of Fig. 12.

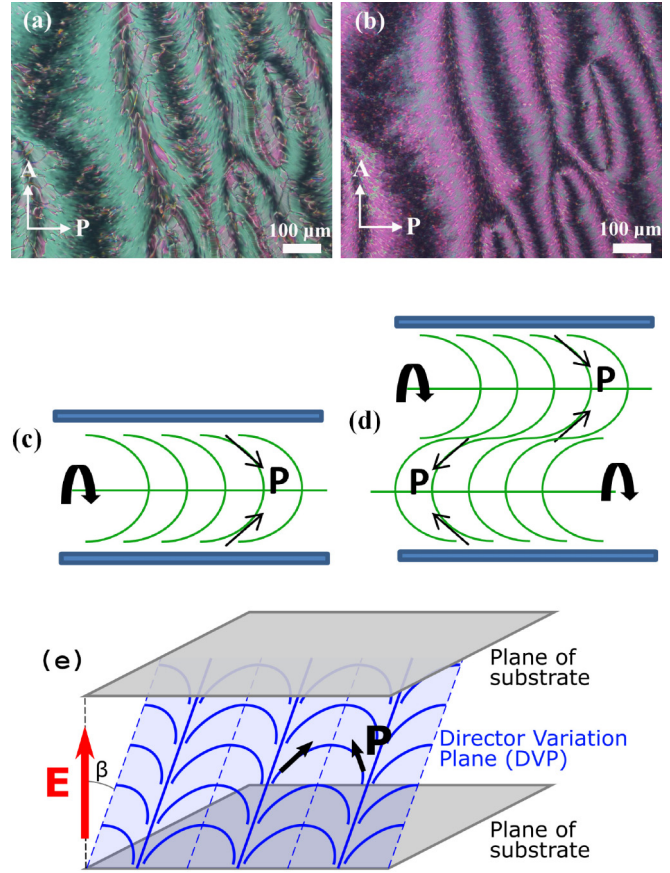


FIG. 4. POM images of quacylindrical domains in  $N_F^{2D}$  (a) and  $N_{AF}$  (b); orientation of planar domains (schematic illustration) in  $N_F^{1D}$  (c) and  $N_{AF}^{1D}$  (d) at  $E = 0$ ; orientation of planar domains in  $N_F^{1D}$  at  $E \neq 0$ . In (a) and (b) DIO material is used; cell thickness is 10  $\mu\text{m}$ . Images of (a) and (b) are reproduced with permission from Ref. [16]. Copyright WILEY-VCH Verlag GmbH & Co. KGaA, Weinheim, 2017.

The 5- $\mu\text{m}$ -thick planar cell was filled with DIO liquid crystal in an isotropic state. After that, the sample was examined by a polarizing optical microscope (Nikon V100N Pol, Japan) equipped with a heating stage (TMS-93 Stage Temp Controller and THMS 600 microscope stage, UK). The voltage from a waveform generator (Agilent 33220A, USA) was applied to the ITO-coated cell substrates.

Upon cooling in the absence of electric field,  $N_{AF}$  is observed between 68.8 and 84.5  $^{\circ}\text{C}$  [16]. The 1 kHz frequency electric field of various amplitude was applied at several temperatures within this range. The images of the structure variation at application of electric field are presented in Fig. 5. From computer simulations (Sec. IV C) it follows that the antiferroelectric splay remains in the plane of the substrate and gradually disappears when the voltage increases, while the ferroelectric splay arises in the direction perpendicular to the glass and gradually increases. Starting from a particular voltage, the stripes corresponding to the director periodic modulation in space rotate from longitudinal (parallel to the rubbing direction) to transverse (perpendicular to the rubbing direction). In the 5- $\mu\text{m}$ -thick planar cell, in correspondence

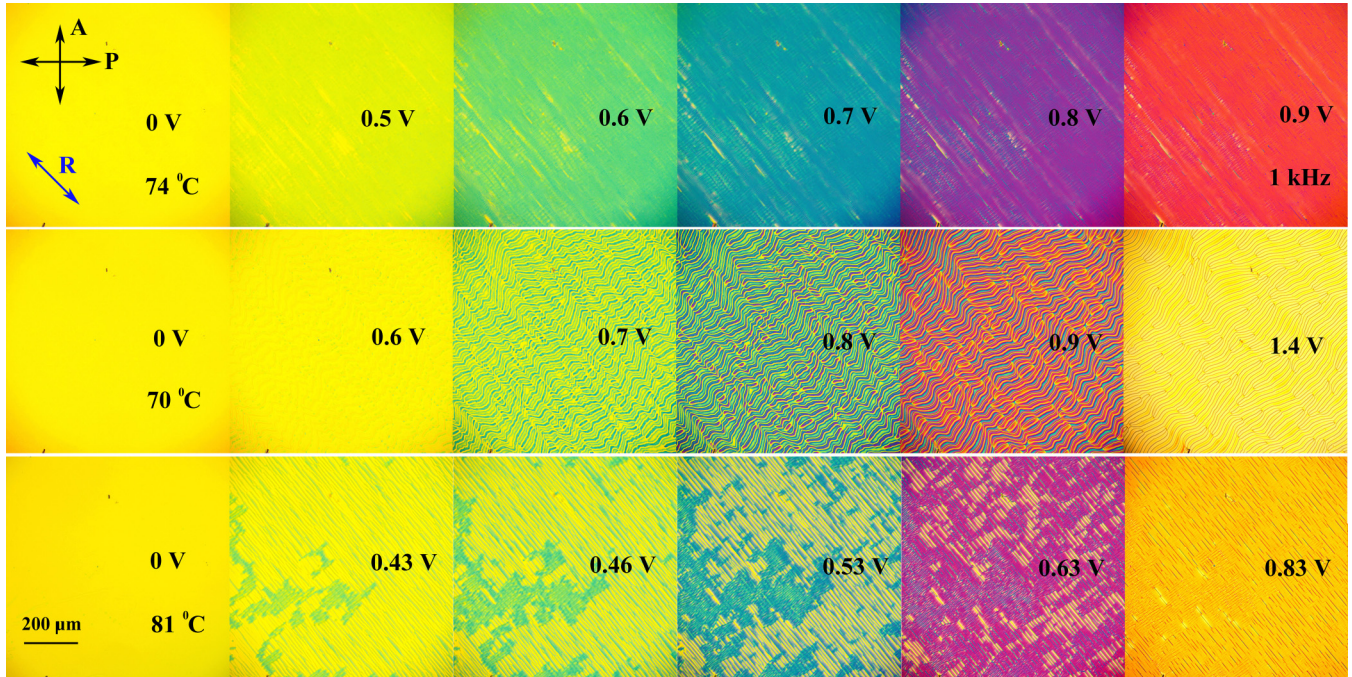


FIG. 5. POM images of the DIO planar cell (cell thickness is 5  $\mu\text{m}$ ) at several voltages (sinusoidal signal, 1 kHz) and temperature  $T = 74^\circ\text{C}$  (Row 1),  $70^\circ\text{C}$  (Row 2), and  $81^\circ\text{C}$  (Row 3). P and A are the directions of polarizer and analyzer, R is the rubbing direction.

with Fig. 3(b), the domains are bigger than the cell thickness almost in the whole temperature range of  $N_{AF}$  and they are therefore suppressed at the ground state (at  $E = 0$ ) by the surfaces. From birefringence measurements in Ref. [35] we also conclude that, at 0 V, the conventional paraelectric nematic phase is observed. Temperature  $74^\circ\text{C}$  (Row 1 in Fig. 5) corresponds to the middle of the temperature range of  $N_{AF}$  in the infinite bulk. At 0.6 V the structure with longitudinal stripes, which is similar to the one obtained in computer simulations, arises. When the voltage increases, one can observe the gradual disappearance of the longitudinal stripes and the appearance of the transverse ones. At  $70^\circ\text{C}$  (Row 2 in Fig. 5) the AF to F transition threshold [Fig. 3(a)] corresponds to the lower voltage, therefore 0.6 V is a sufficiently large voltage to cross over directly to the ferroelectric state, and only the transverse stripes are observed. One notes that at each transverse stripe, the middle of each arc presented in Fig. 4(e) fully satisfies the planar alignment at the vertical orientation of the director variation plane ( $\beta = 0$ ). When the voltage increases, the director modulation first increases, but at higher voltage it starts decreasing again. At  $81^\circ\text{C}$  (Row 3 in Fig. 5) the situation is generally the same. First, the longitudinal stripes appear, then the transverse ones. Surprisingly, at any temperature, at higher voltage the structure is targeted to become planar paraelectric again. This mainly happens due to a disbalance between the induced and flexoelectric polarizations, which is discussed in detail in Sec. IV B.

From experimental observation it also follows that transformation from  $N_F^{2D}$  to  $N_F^{1D}$  induced by electric field also happens continuously, while all the phase borders presented in Fig. 3(a) follow from consideration of simplified geometries (either planar or cylindrical) and rather indicate tentative places on the diagram where the continuous transforma-

tions between phases should happen. In Fig. 6, POM images of a planar cell of DIO material at  $67^\circ\text{C}$  (just below the temperature of transition from  $N_F^{2D}$  to  $N_{AF}$ ) are presented upon application of 0.4 V, 1 kHz electric field. The major part of the cell [Fig. 6(a)] represents a conjugation of  $N_F^{2D}$  cylindrical domains with each other, similar to those presented in Fig. 2(b). Another part of the cell [Fig. 6(b)] demonstrates a continuous transformation from  $N_F^{2D}$  to  $N_F^{1D}$ . The quasicylindrical domains continuously transform into the elongated ones and then to the linear stripes. Here the darker dots and lines correspond to  $\theta \rightarrow 0$  and  $\pi$  (the places where the director is parallel to electric field—at cylinder axes or in the middle planes of planar domains; see the definition of angle  $\theta$  in Fig. 2). The brighter surrounding corresponds to  $\theta \rightarrow \pi/2$  (the places where the director is parallel to the substrate—at the domain periphery). At higher voltage, the whole system transforms into  $N_F^{1D}$  and then into paraelectric  $N$ .

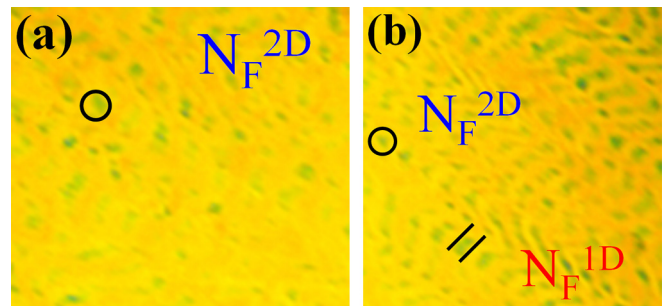


FIG. 6. POM images of the two parts of the cell with DIO at  $67^\circ\text{C}$  under 0.4 V, 1 kHz electric field: (a) mostly  $N_F^{2D}$ ; (b) transformation from  $N_F^{2D}$  to  $N_F^{1D}$ .

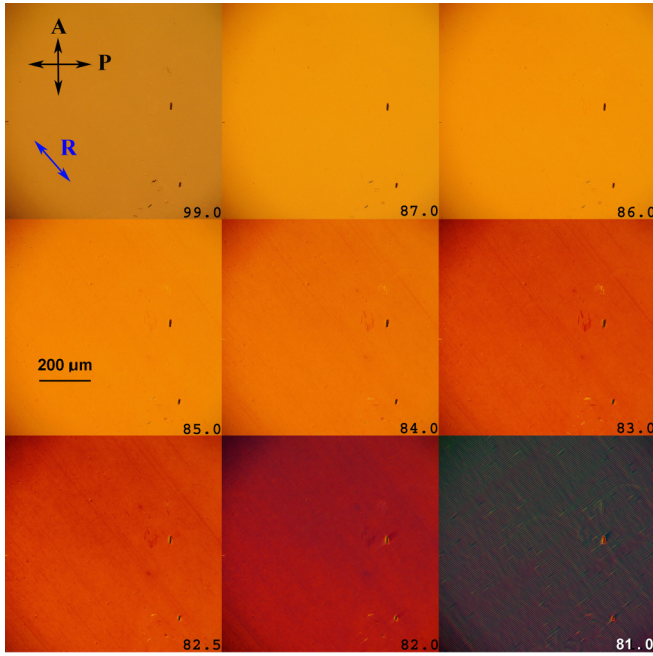


FIG. 7. POM images of the DIO planar cell (cell thickness is 5  $\mu\text{m}$ ) at applied fixed electric field (0.9 V, sinusoidal signal, 1 kHz) during the cooling cycle (temperatures are indicated in the bottom right corners). P and A are directions of polarizer and analyzer, while R is the rubbing direction.

### B. Variation of the structure of DIO on cooling at applied voltage

Let us consider the temperature-induced phase transitions in a polar nematic in the presence of electric field. The 5- $\mu\text{m}$ -thick planar cell filled with DIO material was cooling from 99  $^{\circ}\text{C}$  down to 27  $^{\circ}\text{C}$  at an applied 1 kHz frequency electric field with constant amplitude 0.9 V. The images in crossed polarizers were registered each half-degree. The phase sequence generally appears to be completely different from that observed without electric field. Particular key images are presented in Figs. 7 and 8 (see also Video 1 in the supplemental material [52]). The images practically do not change between 99 and 87  $^{\circ}\text{C}$  (see Fig. 7). Presumably we observe the uniform paraelectric nematic with planar orientation of the director in this temperature range. One notes that our theoretical phase diagram presented in Fig. 3(a) predicts the existence of the  $N_F^{1D}$  polar phase below 93  $^{\circ}\text{C}$ . However, in correspondence with Fig. 3(b), an equilibrium domain length (corresponding to the infinite bulk of LC) in the temperature range between 93 and 87  $^{\circ}\text{C}$  is predicted to be huge, and, in realistic confined geometry, the splay domains are most likely suppressed by the substrates. However, below 87  $^{\circ}\text{C}$  the images start gradually becoming darker, and some longitudinal stripes arise.

The red arrows with numbers presented in Figs. 3(a) and 3(b) reflect the temperatures of particular phase transitions observed in DIO at applied fixed voltage, and Arrow 1 tentatively corresponds to the realistic temperature of transition from paraelectric  $N$  to  $N_F^{1D}$  in DIO confined between parallel glasses (87  $^{\circ}\text{C}$ ). At 87  $^{\circ}\text{C}$  the equilibrium domain size in  $N_F^{1D}$  is still greater than the cell thickness. However, we expect that the highly tilted (almost parallel to the substrate,  $\beta \rightarrow$

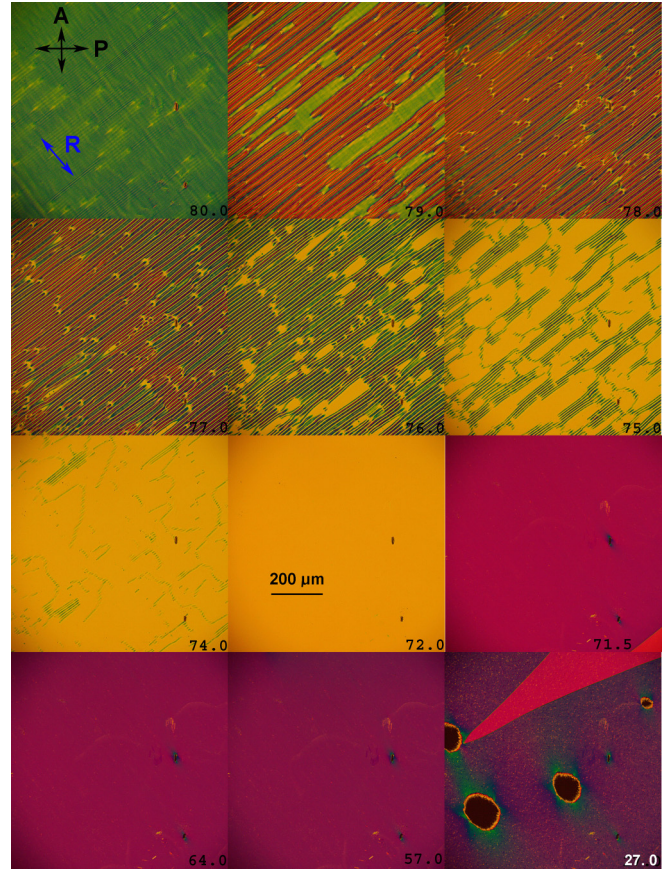


FIG. 8. POM images of the DIO planar cell (cell thickness is 5  $\mu\text{m}$ ) at applied fixed electric field (0.9 V, sinusoidal signal, 1 kHz) during the cooling cycle (continuation of Fig. 7).

$\pi/2$ ) single-splay domains can already exist. The electric field would like to make the director variation plane vertical [perpendicular to the substrates,  $\beta = 0$  in Fig. 4(e)], but in this case the splay domains would not fit the gap between glasses. In this situation, both arms of each arc in Fig. 4(e) choose the longitudinal (parallel to the rubbing) orientation, and this could be the origin of the longitudinal stripes observed in the temperature range between 87 and 82  $^{\circ}\text{C}$ . When the temperature decreases down to 82  $^{\circ}\text{C}$ , the domain size decreases continuously [see Fig. 3(b)], therefore the arcs presented in Fig. 4(e) gain larger and larger vertical projection (which is favorable for the coupling of flexoelectric polarization with electric field), and the images in crossed polarizers are becoming darker and darker.

Surprisingly, the structure variation does not demonstrate any irregular variation near the transition into  $N_{AF}$  registered at 84.5  $^{\circ}\text{C}$  in Ref. [16] by DSC measurements in the absence of electric field, which indirectly indicates that the structure of LC does not have any tendency to return to the ground state between pulses of high-frequency electric field. An easy explanation for this effect is that the switch-off relaxation time should be much longer than the inverse frequency of electric field in this temperature range. This could be related to the fact that flexoelectric polarization inversion requires the director splay inversion in the whole space. However, the director is trapped by its own periodic structure. The alternative to the

director's continuous motion is the total director disruption in the whole space, the energy cost of which is much higher. Since the director is determined on the scale, which is much larger than molecular size, the director motion is analogous to that of the Brownian particles, whose velocity is much slower than molecular velocity. Our expectation following from the Einstein-Smoluchowski equation is that the director should not move faster than several micrometers per second, which means that application of 1 kHz frequency electric field should definitely trap the director distribution within the 5- $\mu\text{m}$ -thick cell, since the director can only move a few nanometers per pulse. If the frequency of electric field is between the inverse  $\tau_{\text{on}}$  and  $\tau_{\text{off}}$ , the director should stay in the position of a particular (say, positive) pulse, and should not return to the ground state between pulses. Detailed analysis of all the images of DIO material obtained at application of the high-frequency electric field demonstrates good correlation with our theoretical predictions obtained in a supposition of constant electric field used in Sec. IV.

The next phase transition [marked with Arrow 2 in Fig. 3(b)] takes place at some temperature between 82 and 81  $^{\circ}\text{C}$  (see Fig. 7), at which the transverse (perpendicular to the rubbing direction) stripes appear, and the whole image becomes darker stepwise. This transition is most likely first-order and is related to the reorientation of the director variation plane [reorientation of each arc presented in Fig. 4(e) around the vertical axis]. The reason is that the vertical projection of each arc is already sufficiently great at 82  $^{\circ}\text{C}$ , and the middle of each arc is targeted to be oriented along the rubbing direction, while the arms of each arc, on the contrary, are not biased anymore.

From observation of images presented in Fig. 8, it follows that between 80 and 79  $^{\circ}\text{C}$  [Arrow 3 in Fig. 3(a)], the transition from  $N_F^{1D}$  to the phase corresponding to  $N_{AF}$  deformed in the electric field (see the discussion in Sec. III A) takes place. Tentatively, the structure variation in this temperature range follows the green arrow in Fig. 3(a), which is inclined, because the splay elastic constant (participating in the denominator of the value plotted on the vertical axis) should tentatively increase with decreasing temperature, at least within the range of a single phase. One can see the islands of  $N_{AF}$  inside of  $N_F^{1D}$  at 80  $^{\circ}\text{C}$ , and therefore the  $N_F^{1D}$  to deformed  $N_{AF}$  phase transition is also of first order.

At about 74  $^{\circ}\text{C}$ , the structure comes out of the  $N_{AF}$  range [Arrow 4 in Fig. 3(a)]. Formally, the structure should return to  $N_F^{1D}$ . However, it was demonstrated in Sec. III A that, at this temperature and voltage, the director splay modulation is not very deep, and the structure rather resembles the paraelectric nematic with planar director orientation. The origin of this effect will be discussed Sec. IV B.

At 71.5  $^{\circ}\text{C}$  the new phase transition happens [Arrow 5 in Fig. 3(b)]. From our observations in Ref. [35] and also from Fig. 3(b) it follows that the size of the domains in  $N_{AF}$  becomes comparable to the cell thickness at around 71.5  $^{\circ}\text{C}$ , and thus the stripes corresponding to the splay domains in  $N_{AF}$  would arise at  $E = 0$ . Above 71.5  $^{\circ}\text{C}$  the structures of DIO at applied voltage and in the ground state are the same—the planar paraelectric nematic, while below 71.5  $^{\circ}\text{C}$  they become different again. The observed structure returns to the one resembling  $N_F^{1D}$  observed between 82 and 87  $^{\circ}\text{C}$  with

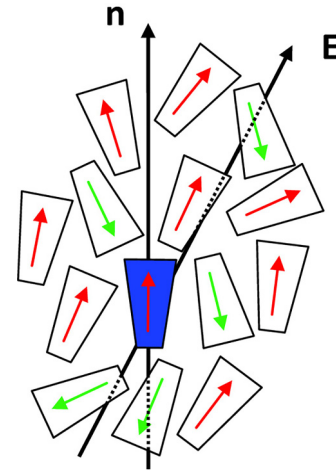


FIG. 9. A trial (blue) polar molecule in a combination of the mean molecular field and electric field  $\mathbf{E}$ . Here  $\mathbf{n}$  is the local director at a point where the trial molecule is located.

partial inclusions of the  $N_F^{2D}$  domains, whose axes (visible as reflecting dots) are oriented parallel to the electric field and perpendicular to the substrates. When the temperature decreases further (see Fig. 8), the images become darker, and the number of reflecting dots increases. The structure variation completely ignores the  $N_{AF}$  to  $N_F^{2D}$  transition registered at 68.8  $^{\circ}\text{C}$  by DSC measurements in Ref. [16] in the absence of electric field, and thus the structure does not return to the ground state again, similarly to that in the temperature range between 82 and 87  $^{\circ}\text{C}$ .

At 57  $^{\circ}\text{C}$  the material structure is already close to the nominal transition into  $N_F^{2D}$ . At 27  $^{\circ}\text{C}$ , the structure corresponding to the quasi-ideal  $N_F^{2D}$  with islands of crystal and also with some domains similar to those reported in Ref. [53], consideration of which is beyond the scope of the present paper, arises. At different temperatures we observe similar domains at application of much higher voltage, at which we already expect an induction of paraelectric nematic phase by electric field (see the discussion in Secs. III A and IV B). One notes that, at planar boundary conditions, in the presence of electric field we obtained an image of  $N_F^{2D}$  similar to that obtained at homeotropic boundary conditions without electric field in Ref. [16].

## IV. THEORETICAL APPROACHES

### A. Molecular-statistical theory: Temperature- and electric-field-dependent distributions of $S$ and $P$ order parameters in space

Let us consider a system of elongated polar molecules (with longitudinal electric dipoles  $\mu$ ) interacting with each other and with external electric field  $\mathbf{E}$  (Fig. 9). Formally, constant electric field participates in all the equations below. Having in mind our discussion in Sec. III B about slow relaxation of director splay, we expect that the structures arising at high-frequency electric field do not differ very much from those obtained at constant electric field. In the general case, director field  $\mathbf{n}(\mathbf{r})$  is inhomogeneous, and the free-energy

density  $\partial F/\partial V$  can be written in the following form [50]:

$$4\pi V_0 \frac{\partial F(\mathbf{r}_1)}{\partial V} = k_B T \int d^2 \mathbf{a}_1 f[(\mathbf{a}_1 \cdot \mathbf{n}_1), \mathbf{r}_1] \ln f[(\mathbf{a}_1 \cdot \mathbf{n}_1), \mathbf{r}_1] + \frac{\sigma_0}{8\pi V_0} \int d^2 \mathbf{a}_1 \int d^2 \mathbf{a}_2 \int d^3 \mathbf{r}_{12} f[(\mathbf{a}_1 \cdot \mathbf{n}_1), \mathbf{r}_1] \times f[(\mathbf{a}_2 \cdot \mathbf{n}_2), \mathbf{r}_2] U_{12}^{ef}(\mathbf{a}_1, \mathbf{a}_2, \mathbf{r}_{12}) - \mu \int d^2 \mathbf{a}_1 f[(\mathbf{a}_1 \cdot \mathbf{n}_1), \mathbf{r}_1] (\mathbf{a}_1 \cdot \mathbf{E}), \quad (5)$$

where  $V_0$  is the bulk occupied by a molecule located at point  $\mathbf{r}_1$  and all its nearest neighbors,  $\sigma_0$  is the average number of neighbors for each molecule,  $f[(\mathbf{a} \cdot \mathbf{n}), \mathbf{r}]$  is the orientational distribution function for molecules having principal axes  $\mathbf{a}$  with respect to director  $\mathbf{n}$  at point  $\mathbf{r}$ ,  $\mathbf{r}_i$  ( $i = 1, 2$ ) are the coordinates of points 1 and 2, where molecules 1 and 2 are located,  $\mathbf{r}_{12}$  is the vector connecting points 1 and 2,  $k_B$  is Boltzmann constant,  $T$  is the temperature,  $U_{12}^{ef}(\mathbf{a}_1, \mathbf{a}_2, \mathbf{r}_{12})$  is the effective pair interaction potential for two molecules with long axes  $\mathbf{a}_1$  and  $\mathbf{a}_2$  located at points 1 and 2, respectively, while  $\mathbf{n}_1$  is the director at point 1 and  $\mathbf{n}_2$  is the director at point 2. The first term in Eq. (5) is the minus entropy, the second term is the internal energy, and the third term is the energy of interaction of molecular longitudinal dipoles with electric field. At any point  $\mathbf{r}$ , the orientational distribution function  $f[(\mathbf{a} \cdot \mathbf{n}), \mathbf{r}]$  in Eq. (5) satisfies the normalizing constraint:

$$\int d^2 \mathbf{a} f[(\mathbf{a} \cdot \mathbf{n}(\mathbf{r})), \mathbf{r}] = 1. \quad (6)$$

Minimizing the free energy (5) with respect to the orientational distribution function  $f[(\mathbf{a} \cdot \mathbf{n}), \mathbf{r}]$  under constraint (6), one obtains

$$f[(\mathbf{a} \cdot \mathbf{n}), \mathbf{r}] = \frac{1}{I_0(\mathbf{r})} \exp \left\{ - \frac{U_{MF+E}[(\mathbf{a} \cdot \mathbf{n}), \mathbf{r}]}{k_B T} \right\}, \quad (7)$$

where  $\mathbf{r} \equiv \mathbf{r}_1$ ,  $\mathbf{n} \equiv \mathbf{n}_1$ ,  $I_0(\mathbf{r})$  is the normalizing constant, and  $U_{MF+E}[(\mathbf{a} \cdot \mathbf{n}), \mathbf{r}]$  is the potential of a molecule located at point  $\mathbf{r}$  with orientation  $\mathbf{a} \equiv \mathbf{a}_1$  of the prime axis in a combination of the mean molecular field and electric field:

$$U_{MF+E}[(\mathbf{a} \cdot \mathbf{n}), \mathbf{r}] \equiv \frac{\sigma_0}{4\pi V_0} \int d^3 \mathbf{r}_{12} \int d^2 \mathbf{a}_2 f[(\mathbf{a}_2 \cdot \mathbf{n}_2), \mathbf{r}_2] \times U_{12}^{ef}(\mathbf{a}, \mathbf{a}_2, \mathbf{r}_{12}) - \mu (\mathbf{a} \cdot \mathbf{n})(\mathbf{n} \cdot \mathbf{E}). \quad (8)$$

Approximating the pair potential by spherical invariants [Eq. (1)], substituting Eq. (1) into Eq. (8), introducing coefficients

$$J_{\ell L \lambda}^{(i)} \equiv \frac{\sigma_0}{V_0} \int_0^\infty dr_{12} r_{12}^{i+2} J_{\ell L \lambda}(r_{12}), \quad (9)$$

and using only  $T_{101}$ ,  $T_{110}$ ,  $T_{011}$ , and  $T_{202}$  spherical invariants resulting on the average in the appearance of the terms in the mean field depending on the powers of operator  $\nabla$  not higher than 1, one finally obtains the following expression for the potential of a molecule with orientation  $\mathbf{a}$  affected by a combination of the mean molecular field and electric field:

$$-U_{MF+E}(t, \mathbf{r}) = J_{101}^{(0)} P(\mathbf{r}) P_1(t) + J_{202}^{(0)} S(\mathbf{r}) P_2(t) + \left\{ \frac{1}{6} \left[ J_{110}^{(1)} + J_{011}^{(1)} \right] (\nabla \cdot \mathbf{n}) + \mu (\mathbf{n} \cdot \mathbf{E}) \right\} P_1(t), \quad (10)$$

where  $t \equiv (\mathbf{a} \cdot \mathbf{n})$ , and  $P_1(t) \equiv t$  and  $P_2(t) \equiv 3/2 t^2 - 1/2$  are the first and second Legendre polynomials. Equation (10) corresponds to the first (simplest) approximation reflecting modulation of the  $S$  and  $P$  order parameters caused by modulation of splay and describing the major tendency: both parameters  $S$  and  $P$  should be higher (lower) at the places where the splay is higher (lower). The first two terms in Eq. (10) are the polar and nonpolar anisotropies, while the two terms in brackets are due to the flexoelectric effect and electric field. From Eqs. (2), (7), and (10) one readily obtains the following recurrent equations for determination of the  $P(\mathbf{r})$  and  $S(\mathbf{r})$  order parameters at each temperature  $T$  and electric field  $E$  at any given  $\mathbf{n}(\mathbf{r})$  distribution:

$$P(\mathbf{r}) = \frac{I_1(\mathbf{r})}{I_0(\mathbf{r})}, \quad S(\mathbf{r}) = \frac{I_2(\mathbf{r})}{I_0(\mathbf{r})}, \quad (11)$$

where integrals  $I_m(\mathbf{r})$  are defined as follows:

$$I_m(\mathbf{r}) \equiv \int_{-1}^1 P_m(t) \exp \left\{ - \frac{U_{MF+E}(t, \mathbf{r})}{k_B T} \right\} dt, \quad (12)$$

where  $U_{MF+E}$  is determined by Eq. (10). Substituting solution (7)–(10) back into Eq. (5), one obtains for the equilibrium free-energy density  $\partial F_{eq}/\partial V$ :

$$4\pi V_0 \frac{\partial F_{eq}(\mathbf{r})}{\partial V} = -k_B T \ln I_0(\mathbf{r}) + \frac{1}{2} J_{101}^{(0)} P^2(\mathbf{r}) + \frac{1}{2} J_{202}^{(0)} S^2(\mathbf{r}), \quad (13)$$

where normalizing integral  $I_0(\mathbf{r})$  should be calculated using Eqs. (12) and (10). Equation (13) should be used for comparison of the free energies of the neighboring phases in the phase diagram.

As was mentioned in Sec. II, Eq. (4) (multiplied by  $4\pi V_0$ ) is the part of Eq. (5) explicitly dependent on director  $\mathbf{n}$ . Indeed, if one prolongs the gradient expansion in Eq. (10) up to the terms depending on the second power of operator  $\nabla$  [for this purpose, invariants  $T_{220}$ ,  $T_{022}$ ,  $T_{222}$ ,  $T_{422}$ , and  $T_{224}$  should also be considered in approximation Eq. (1)]; this is done in Ref. [50]] and substitutes Eq. (10) into the second and third terms of Eq. (5) [definition Eq. (8) should also be used], then one obtains Eq. (4). In particular, the flexoelectric and electric-field-dependent terms (which explicitly depend on both  $P$  and  $\mathbf{n}$ ) coincide in Eqs. (4) and (5) at substitution of  $4\pi V_0 K_{11\lambda} = [J_{110}^{(1)} + J_{011}^{(1)}]/6$  and  $4\pi V_0 \epsilon_a = \mu$ . By the same substitution of Eq. (10) into Eq. (5), one obtains the  $P^2$  term introduced phenomenologically in Ref. [38]. In the same manner, it is possible to obtain additional contributions to the elastic constants depending on the polar order parameter  $P$  studied phenomenologically in Refs. [19,38] (see also Ref. [35]).

### B. Perturbation elastic continuum theory reflecting space variation of $S$ and $P$ order parameters

Let us now consider the director distribution in the polar phases in the presence of electric field, having in mind the results obtained in Sec. IV A. In the cases presented in Figs. 2(a) and 2(b), we expect that the director is (mostly) along the radial planes (the planes parallel to the cylinder axis  $\mathbf{x}$  and radius  $\mathbf{r}$ ). Thus, in all cases presented in Fig. 2, the director mainly has two nonzero coordinates, similarly to that in Ref. [54]:

$$n_x = \cos \theta(r), \quad n_r = \sin \theta(r). \quad (14)$$

One notes that all the structures presented in Fig. 2 can be described in a unified way, and here we also introduce the  $\delta$  parameter to distinguish between the double- and single-splay structures ( $\delta$  is set to 1 in the case of 2D-splay and is set to 0 in the case of 1D-splay). From Eq. (14) it follows that

$$\begin{aligned} (\nabla \cdot \mathbf{n}) &= \frac{\delta}{r} \sin \theta + \cos \theta \frac{d\theta}{dr}, \\ [\mathbf{n} \times [\nabla \times \mathbf{n}]]^2 &= \sin^2 \theta \left( \frac{d\theta}{dr} \right)^2. \end{aligned} \quad (15)$$

In the manner of paper [35], let us consider the one-constant approximation  $K_{11} = K_{33} \equiv K$  for simplicity. An equilibrium director  $\mathbf{n}(\mathbf{r})$  distribution should be obtained by independent minimization of free-energy density (4), while an equilibrium polarization  $P(\mathbf{r})$  distribution has already been obtained by independent minimization of free-energy density (5) and is presented by Eq. (11). Precise minimization of Eq. (4) with constraint (11) appears to be complicated. The complexity is in the fact that minimization with respect to director  $\mathbf{n}$  and polarization value  $P$  should be done independently, while distributed in the space polarization  $P$  (and this distribution is unknown before we know the distribution of  $\mathbf{n}$ ) participates in differential Eq. (4), from where this distribution of  $\mathbf{n}$  is supposed to be obtained. For this purpose, let us consider a perturbation theory based on the assumption that variation of the order parameters in space is small. In the framework of perturbation theory, let us first consider the uniform polarization  $P(\mathbf{r}) = P^*$  in Eq. (4). In both cases of ferroelectric domains presented in Figs. 2(b) and 2(c), let us consider variation of angle  $\theta$  from zero (at the  $\mathbf{x}$ -axis of one domain) to  $\pi$  (at the  $\mathbf{x}$ -axis of the neighboring domain). Then the same simplification for the free-energy density is valid for all the structures presented in Fig. 2: all the terms proportional either to  $d\theta/dr$  or to  $\lambda$  should have opposite signs in the neighboring domains, and the corresponding terms vanish on average. Taking this into account, substituting Eq. (15) into Eq. (4), and minimizing free-energy density (4) with respect to  $\theta$  and  $d\theta/dr$ , as presented, for example, in Ref. [55], Appendix A, one obtains the following equation of state:

$$\left( \frac{d\theta}{dr} \right)^2 + \tau^2 |\cos \theta| - \frac{\delta}{r^2} \sin^2 \theta = \frac{\tau^2}{k^2}, \quad (16)$$

where  $\tau \equiv \sqrt{2\varepsilon_a E P^* / K}$  is the reduced electric field, and  $k$  is some constant independent of angle  $\theta$ , which should be obtained by independent minimization of the free-energy density. Introducing new dimensionless variable  $\psi \equiv \tau r/k$ , one

obtains from Eq. (16)

$$\frac{d\theta}{d\psi} = \sqrt{1 - k^2 |\cos \theta| + \delta / \psi^2 \sin^2 \theta}. \quad (17)$$

Radius  $r_m$  of the domain can now be found by minimization of the free energy with respect to parameter  $k$ . This, however, can be done in a more precise way by partially taking into account the nonuniformity of  $P(\mathbf{r})$ . Indeed, from Eq. (11) it approximately follows [after expansion of the exponent in Eq. (12) in Taylor series with substitution of Eq. (10)] that  $P(\mathbf{r}) \sim (\nabla \cdot \mathbf{n}) + \varepsilon_a E \cos \theta / (K\lambda)$ , where the first term is flexoelectric polarization and the second term is induced by electric field polarization. One notes from Eq. (4) that any rescale of coordinate  $r$ , at which  $r\lambda P$  and  $\tau/(\lambda P)$  remain constant, does not change the free-energy density. This means in the end that distribution of polarization is determined only by distribution of angle  $\theta$  in the space. Let us therefore write the following trial approximation for the polar order parameter:

$$\begin{aligned} P(\theta) &= P^* r_m \{ (\nabla \cdot \mathbf{n}) + \tau^2 \cos \theta / (2\lambda P^*) \} \\ &= P^* \psi_m \left\{ \frac{\delta}{\psi} \sin \theta + \cos \theta \left( \frac{d\theta}{d\psi} + \frac{1}{2} k \tilde{\tau} \right) \right\}. \end{aligned} \quad (18)$$

where  $\tilde{\tau} \equiv \tau/(\lambda P^*)$  is the dimensionless electric field. One notes from Eq. (18) that, in the case of  $N_F^{2D}$ , the  $P^*$  proportionality coefficient coincides with  $P$  at  $\theta = \pi/2$  (polar order parameter at periphery  $r_m$  of the ferroelectric domain). In the cases of  $N_F^{2D}$  and  $N_{AF}$ , the  $P^*$  coefficient formally corresponds to a different place  $r^*$  within the domain, other than periphery  $r_m$ . Regardless of the kind of domain, however, the expression in brackets in the first line of Eq. (18) is equal to  $1/r_m$  at  $r^*$ . Substituting Eqs. (15), (17), and (18) into Eq. (4), integrating the free-energy density along the radius of domain (with the  $r dr$  Jacobian for 2D-splay or with the  $dr$  Jacobian for 1D-splay), and dividing the result by the cross section area (for 2D-splay) or by the length of domain (for 1D-splay), one obtains the expression for the average free-energy density, which should be further minimized with parameter  $k$ . This could be done for each polar nematic phase similarly to that presented in Ref. [35] for  $N_{AF}$ . Subsequently, at any value of  $\tilde{\tau}$ , the  $r(\theta)$  dependence can be obtained, and, in particular, radius  $r_m$  of the domain can be obtained. In  $N_{AF}$ ,  $r_m \lambda P^* \approx 1.55$  and maximum tilt is  $\theta_m \approx 64^\circ$ . In  $N_F^{1D}$  and  $N_F^{2D}$ , radius  $r_m$  of the domain generally depends on the applied electric field, while maximum tilt is always equal to  $\theta = \pi/2$ . Several  $\theta(r)$  and  $(\nabla \cdot \mathbf{n})$  dependencies at several particular values of dimensionless electric field  $\tilde{\tau}$  are presented in Figs. 10(a) and 10(b), respectively, for  $N_F^{2D}$  [blue curves (1) and (2)] and  $N_F^{1D}$  [red curves (3), (4), and (5)]. One notes that the tilt of the director varies almost linearly in both  $N_F^{2D}$  and  $N_F^{1D}$ , with a slight tendency to greater variation in the middle of each domain in  $N_F^{2D}$  and, oppositely, at the domain periphery ( $r = r_m$ ) in  $N_F^{1D}$ . From Fig. 10 it follows that, at moderate values of electric field, the maximum splay deformation in  $N_F^{1D}$  is achieved at  $\theta = 0$ , at which the director is parallel to electric field. This is the configuration at which both flexoelectric and induced polarizations give an optimal summarized contribution to the free energy. Therefore, both  $N_F^{2D}$  and  $N_{AF}$  exhibit a transition into  $N_F^{1D}$  at application of electric field. However, there always exists a disbalance between the induced and flexoelectric

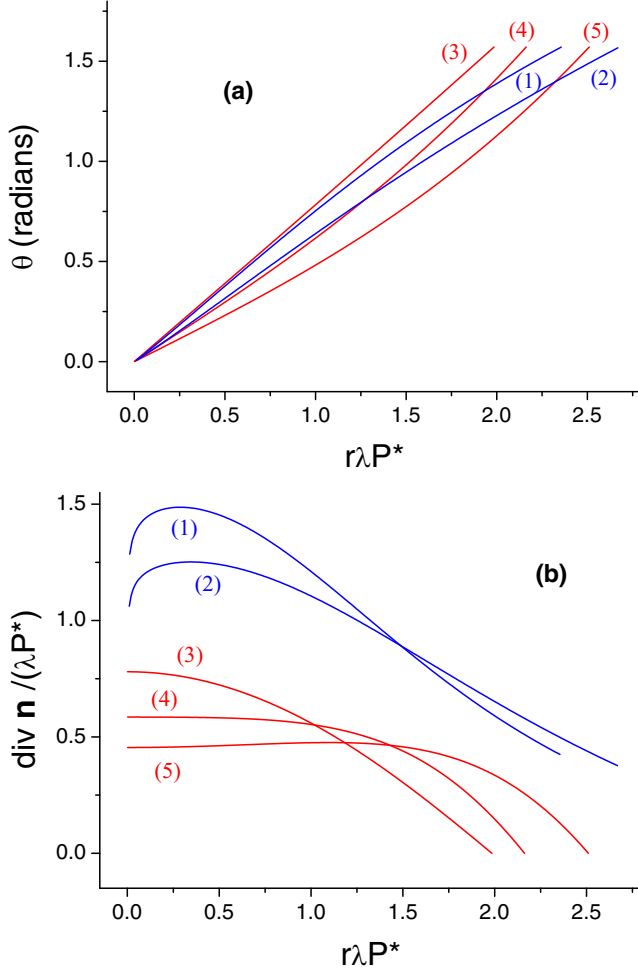


FIG. 10. Tilt of director (a) and splay deformation (b) distributions within the domain in  $N_F^{2D}$  [blue curves (1) and (2)] and  $N_F^{1D}$  [red curves (3), (4), and (5)]. Here  $\tilde{\tau} = 0.001$  (1), 0.22 (2), 0.225 (3), 0.8 (4), and 0.843 (5).

polarizations. Indeed, the flexopolarization can exist only in the presence of director deformation. However, at the application of electric field, the structure becomes more uniform, and the splay deformation reduces. Therefore, at higher electric field, the maximum in Fig. 10(b) reduces and shifts to the position where the director is not parallel to electric field. At  $\tilde{\tau} \approx 0.843$ , the splay phase becomes unstable, and a transition into a paraelectric nematic phase happens. The electric field dependencies of characteristic polar order parameter  $P^*$  and domain radius  $r_m$  at particular fixed temperatures within  $N_F^{1D}$  are presented in Figs. 11(a) and 11(b), respectively. Both dependencies are generally not monotonic because of the non-trivial correlation between splay and electric field. At higher values of electric field,  $P^*$  greatly decreases and  $r_m$  greatly increases just before the transition into  $N$ .

Knowing the director distribution in space in  $N_F^{2D}$ ,  $N_{AF}$ , and  $N_F^{1D}$ , one obtains the distributions of  $S$  and  $P$  order parameters in each phase using Eqs. (10)–(12). For this purpose, one should substitute approximation (18) into the last line of Eq. (10). In particular, at specific places  $r^*$  within each domain, where polar order parameter  $P$  coincides

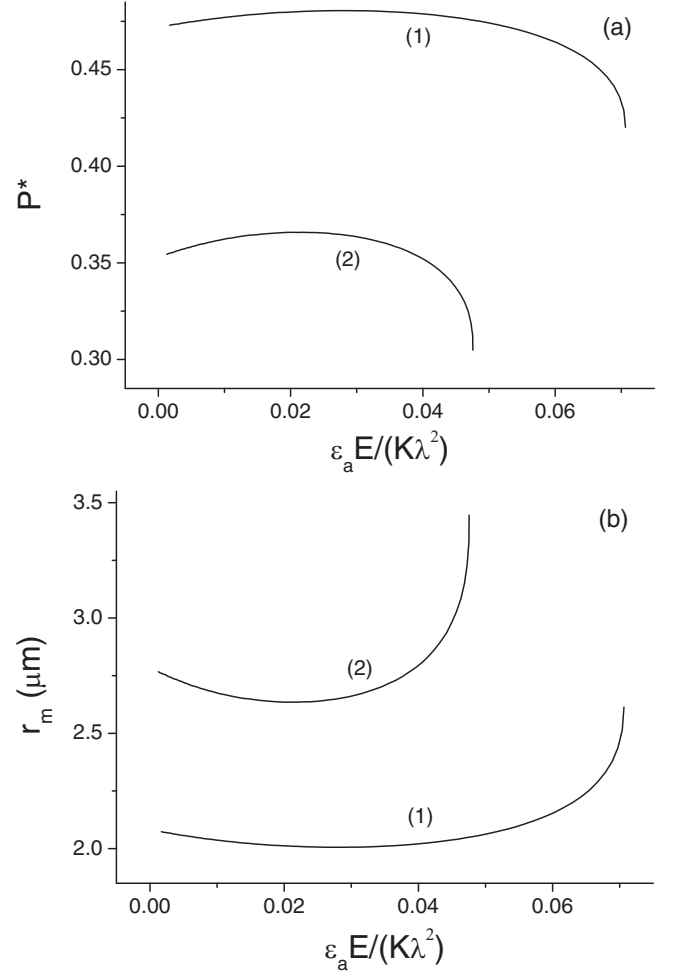


FIG. 11. Electric field dependencies of the characteristic polar order parameter (a) and domain radius (b) in  $N_F^{1D}$  at  $J_{202}^{(0)}/k_B = 2032$  K,  $J_{101}^{(0)}/k_B = 362$  K,  $\lambda = 2 \mu\text{m}^{-1}$ ,  $K V_0 = 5 \times 10^{-35} \text{ N m}^3$ , and  $T = 70^\circ\text{C}$  [curves (1)] and  $81^\circ\text{C}$  [curves (2)].

with coefficient  $P^*$ , one immediately obtains that the whole expression in brackets in the last line of Eq. (10) is equal to  $[J_{110}^{(1)} + J_{011}^{(1)}]/(6r_m)$ . From the recurrent Eqs. (11) and (12) one obtains  $S^*$  and  $P^*$  first, and then the whole distribution of  $S(r)$  and  $P(r)$  within the domain, which are presented in Fig. 12. One notes that both  $S$  and  $P$  generally decrease with increasing temperature. The maximal values of both parameters are observed close to the middle of the domain in  $N_F^{2D}$  and  $N_{AF}$  and in the middle exactly in  $N_F^{1D}$ . The polar order parameter reaches zero at the periphery of each domain in  $N_F^{1D}$ , while in  $N_F^{2D}$  and  $N_{AF}$  it does not, which means that flexopolarization exhibits stepwise reversal between the domains without director disruption. Distributions of  $S(r)$  and  $P(r)$  at several nonzero values of electric field are also presented in Fig. 13. One notes that profiles of both  $S$  and  $P$  first tend to become sharper at moderate electric field and then smoother at higher electric field.

### C. Computer simulations

To perform calculations of director distribution in a polar nematic film under the action of an electric field, we have modified the existing extended Frank elastic continuum

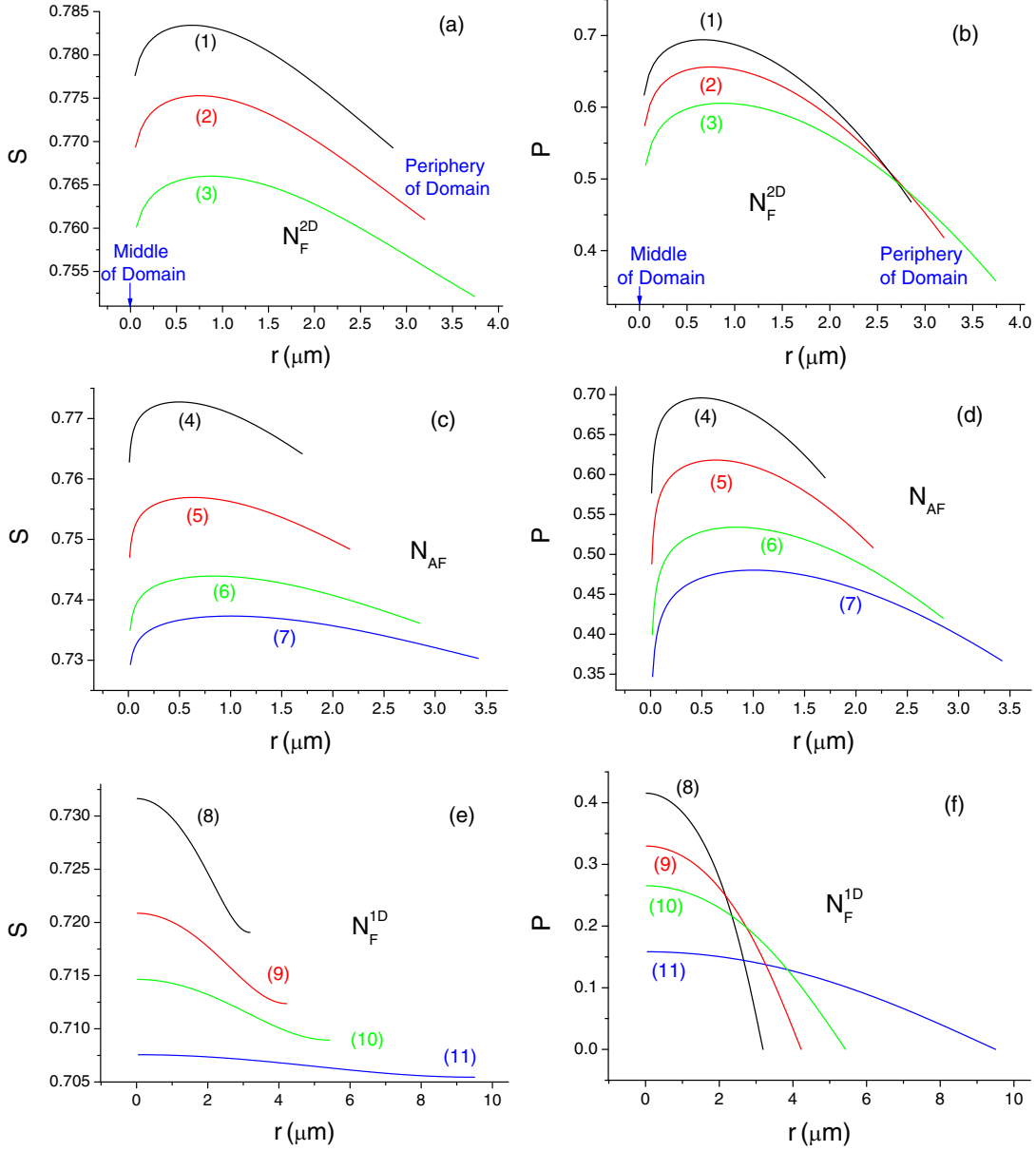


FIG. 12. Distribution of the  $S$  [(a),(c),(e)] and  $P$  [(b),(d),(f)] orientational order parameters within the domains in  $N_F^{2D}$  [(a),(b)],  $N_{AF}$  [(c),(d)], and  $N_F^{1D}$  [(e),(f)] at  $T = 57^\circ\text{C}$  (1);  $62^\circ\text{C}$  (2);  $67^\circ\text{C}$  (3);  $69^\circ\text{C}$  (4);  $76^\circ\text{C}$  (5);  $81^\circ\text{C}$  (6);  $83^\circ\text{C}$  (7);  $85^\circ\text{C}$  (8);  $88^\circ\text{C}$  (9);  $90^\circ\text{C}$  (10); and  $92^\circ\text{C}$  (11) at  $E = 0$ ,  $J_{202}^{(0)}/k_B = 2032\text{ K}$ ,  $J_{101}^{(0)}/k_B = 362\text{ K}$ ,  $\lambda = 2\ \mu\text{m}^{-1}$ ,  $J_A/k_B = 113\text{ K}\ \mu\text{m}$ , and  $KV_0 = 5 \times 10^{-35}\text{ N m}^3$ . Radius  $r$  is defined in Fig. 2 for all the polar phases. Here  $J_A$  is the strength of antiferroelectric decoupling [35,56].

approach [35], previously used for calculations of polar nematic material. The original approach takes into account the effects of director field distortion with the  $\lambda(\mathbf{n} \cdot \mathbf{p})$  term in-

cluded, as well as the formation of defects and finite energy of the surface boundaries. In this paper, we have modified the free energy to take into account the action of an electric field:

$$\begin{aligned}
 F = & \frac{1}{2} \int_V \{K_{11}[\mathbf{n}(\nabla \cdot \mathbf{n}) - \lambda \mathbf{p}]^2 + K_{22}(\mathbf{n} \cdot [\nabla \times \mathbf{n}])^2 + K_{33}[\mathbf{n} \times [\nabla \times \mathbf{n}]]^2\} dV \\
 & - \varepsilon_a \int_V (\mathbf{n} \cdot \mathbf{p})(\mathbf{n} \cdot \mathbf{E}) dV + \frac{W}{2} \int_\Omega (1 - \cos^2 \gamma) d\Omega + F_{\text{def}},
 \end{aligned} \tag{19}$$

where  $K_{11}$ ,  $K_{22}$ , and  $K_{33}$  are the splay, twist, and bend elastic constants, respectively,  $K_{11}\lambda$  is the flexoelectric constant,  $\mathbf{p}$

is the polarizability direction vector,  $\mathbf{E}$  is the electric field intensity,  $V$  is the bulk of the sample having surface  $\Omega$ ,  $W$  is

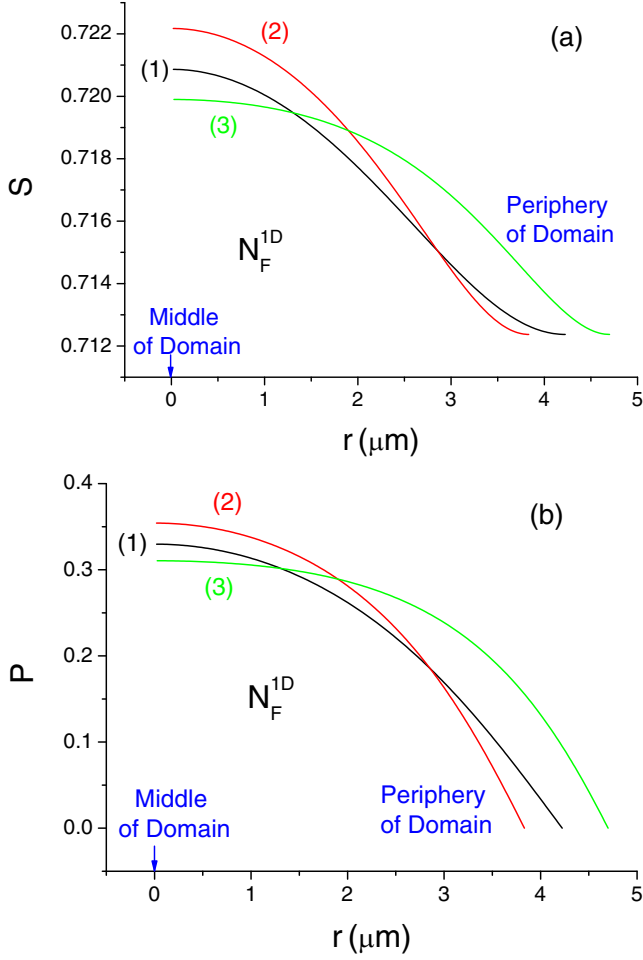


FIG. 13. Distribution of the  $S$  (a) and  $P$  (b) orientational order parameters within the domains in  $N_F^{1D}$  at  $\varepsilon_a E / (K\lambda^2) = 0$  (1); 0.01 (2); 0.028 (3) at  $T = 87^\circ\text{C}$ ,  $J_{202}^{(0)}/k_B = 2032\text{ K}$ ,  $J_{101}^{(0)}/k_B = 362\text{ K}$ ,  $\lambda = 2\ \mu\text{m}^{-1}$ , and  $KV_0 = 5 \times 10^{-35}\text{ N m}^3$ . Radius  $r$  is defined in Fig. 2(c).

the surface anchoring energy density,  $\gamma$  is the angle between local director and normal to the surface, and  $F_{\text{def}}$  is the energy of defects calculated by the summation of the point and linear defect energies (see the details in Ref. [57]). The details of optimization are presented in Ref. [35]. For simplicity, polarizability direction vector  $\mathbf{p}$  is supposed to be a unit vector parallel or antiparallel to  $\mathbf{n}$  in each point. In addition, in correspondence with the theoretical part of the paper, an algorithm accepted only those steps with  $(\mathbf{n} \cdot \mathbf{p})(\mathbf{n} \cdot \mathbf{E}) \geq 0$ . As a result, our simulation annealing procedure leads to minimization of the free energy over both director  $\mathbf{n}$  and polarizability direction  $\mathbf{p}$  distributions in a self-consistent way.

The one-constant approximation was used for simplicity:  $K_{11} : K_{22} : K_{33} = 1 : 1 : 1$ , and the value of  $\lambda$  is set to 10. To take into account the potential formation of disclination lines, their core linear energy density was set to  $f_{\text{core}}^{\text{line}} = 10K_{11}$ . The cubic simulation box of size  $0.125 \times 2 \times 2$  was rendered into a  $4 \times 64 \times 64$  lattice. For  $x$  and  $y$  facets, the periodic boundary conditions were applied. For  $z$  facet, planar aligned boundary conditions were set with the rubbing direction having an angle  $\varphi \in [0^\circ; 90^\circ]$  with the  $x$  axis and  $\mu_1 =$

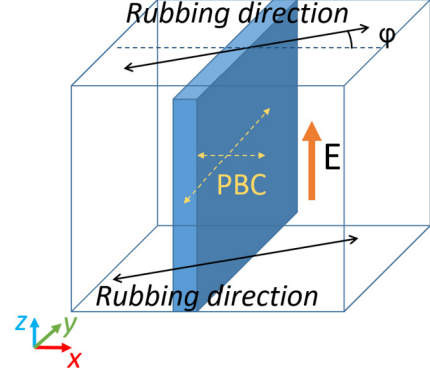


FIG. 14. Principal geometry of the simulations box and the polar nematic film. Black arrows show the rubbing direction of planar alignment of the film. Orange arrow shows the electric field direction. Yellow dashed arrows show the periodic boundary condition directions of the simulation box.

$Wd/K_{11} = 400$ , where  $d$  is the film thickness (see Fig. 14). The electric field  $\mathbf{E}$  was oriented perpendicular to the film plane, and the value of dimensionless electric field intensity  $e = Ed(\frac{\varepsilon_a}{K_{11}})^{1/2}$  varied from 0.1 to 30. For each  $e$ , we produced  $6.1 \times 10^{10}$  steps ( $3 \times 10^7$  parallel multisteps) Monte Carlo annealing optimization with four independent runs to find the energy-optimal structures.

The resulting structures strongly depend on the value of electric field and the rubbing direction  $\varphi$ . Figure 15 shows the dependency of the total free energy of the system on these two parameters. At low values of the electric field ( $e$  from 0.1 to 14), the energy-optimal structure corresponds to the antiferroelectric splay in the  $xy$  plane (which is supposed to be the plane of the substrate in a real experiment) with an alternating sign of polarizability. The average director orientation is almost parallel to the rubbing direction. Some slight ferroelectric modulation is also present: a projection

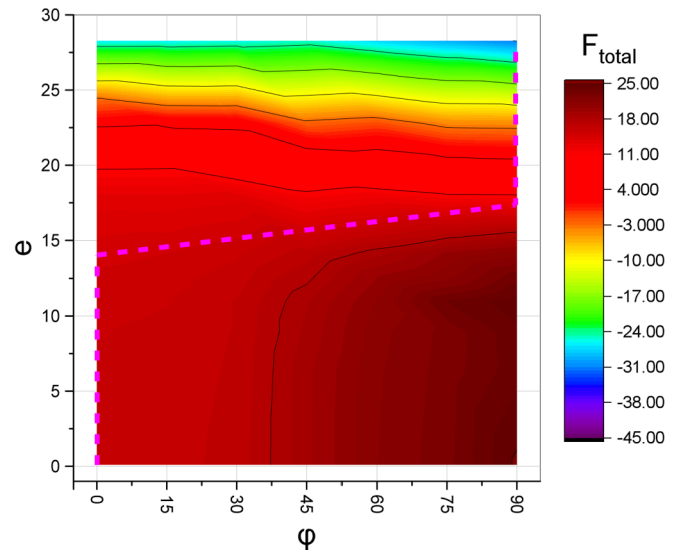


FIG. 15. Dependence of the total free energy on the value of dimensionless electric field  $e$  and rubbing direction orientation  $\varphi$ . Violet dashed line traces energy minimum over  $\varphi$ .

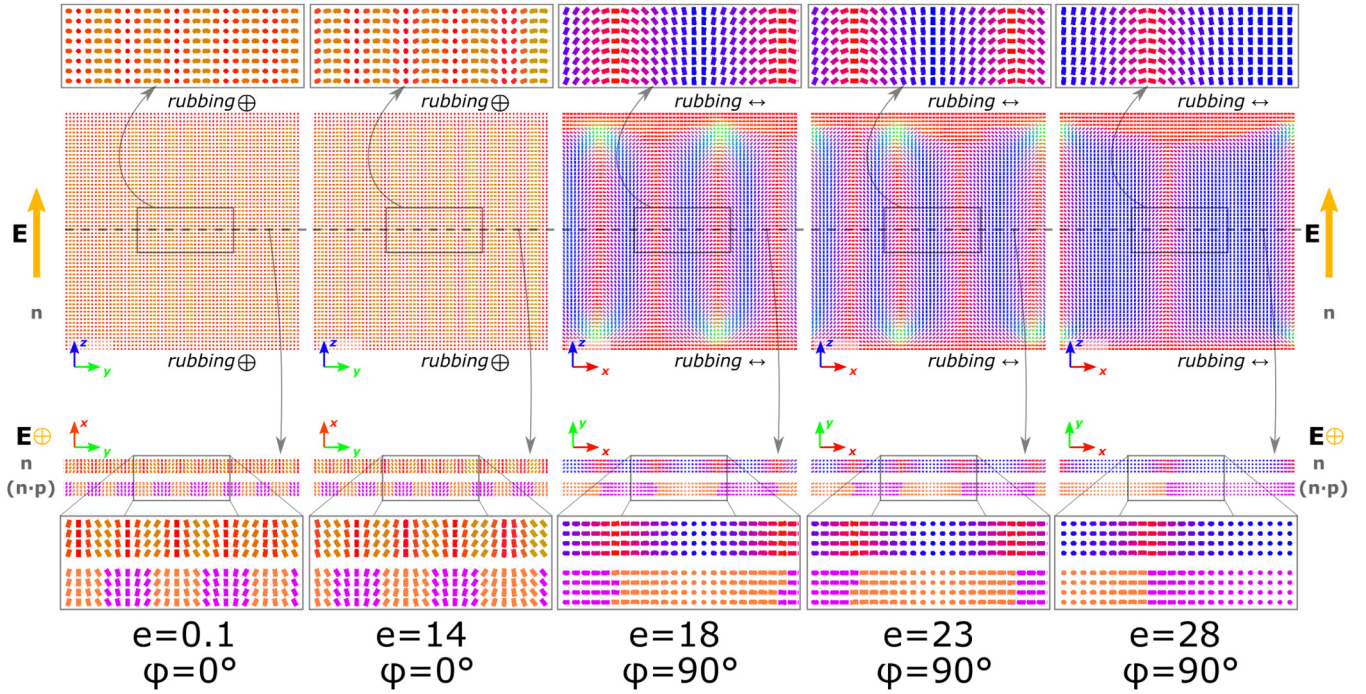


FIG. 16. Director  $\mathbf{n}$  and polarizability  $(\mathbf{n} \cdot \mathbf{p})$  distributions at various dimensionless electric field  $e$  values in the central cross-cuts perpendicular to the substrate plane (top) and along the substrate plane (bottom). Director distributions are shown in color, corresponding to the direction of  $\mathbf{n}$  ( $x$ , red;  $y$ , green;  $z$ , blue). Polarizability is shown in orange [ $(\mathbf{n} \cdot \mathbf{p}) = 1$ ] and violet [ $(\mathbf{n} \cdot \mathbf{p}) = -1$ ].

of the director along electric field arises at the periphery of each antiferroelectric domain, so that the projection of director lines perpendicular to  $xy$  plane gains the shape of periodic arcs. This structure is visualized as longitudinal to the rubbing direction stripes (Fig. 16). Above the threshold value  $e^* \approx 15$ , the system undergoes a transition related to the reorientation of the arcs along the rubbing direction, and the arcs themselves become much bigger, while the antiferroelectric modulation in the  $xy$  plane disappears. This structure (at  $e > 15$ ) is visualized as transverse to the rubbing direction stripes (Fig. 16). At further increasing electric field, the layer period starts growing [similarly to that in theory; see Fig. 11(b)], and the director divergence in the middle of each domain decreases [similarly to that in theory; see Fig. 10(b)]. Computer simulations describe well the transformation from antiferroelectric to ferroelectric structure with the reorientation of stripes, which is observed experimentally and presented in Sec. III A.

## V. CONCLUSION

The origin and structures of ferroelectric and antiferroelectric splay nematic phases are outlined. The double-splay ferroelectric  $N_F^{2D}$  and antiferroelectric  $N_{AF}$  nematic phases are composed of quasicylindrical periodic domains. Without electric field,  $N_F^{2D}$  and  $N_{AF}$  are observed in the lower-temperature range. The single-splay ferroelectric  $N_F^{1D}$  nematic phase is composed of planar periodic domains. Without electric field,  $N_F^{1D}$  is observed in the higher-temperature range. In the presence of electric field, all the splay nematic phases first (at moderate electric field) transform into  $N_F^{2D}$  and then (at higher electric field) into paraelectric nematic phase  $N$  having

uniform director orientation. The origin of all the splay nematic phases is the flexoelectric effect due to the polarity of molecules. The origin of the transformations between phases in electric field is the nontrivial interplay between flexoelectric and induced polarizations. The distribution of the director and both polar  $P$  and nonpolar  $S$  orientational order parameters within the domains of all the splay nematic phases is found. Variation of the structure and properties of the splay nematic phases with variation of temperature and electric field are investigated. The electric field–temperature phase diagram is obtained. The equilibrium domain size was found to increase, and polarization was found to decrease in each polar phase with increasing temperature. Several additional phase transitions related to optimization of the domains within the cell gap were found and explained.

## ACKNOWLEDGMENTS

A.V.E. and V.Yu.R. thank the Russian Foundation for Basic Research (Project No. 21-53-50008) for the financial support of the theoretical investigation presented in this work. S.A.Sh. acknowledges partial support of the experimental investigation presented in this work from M. V. Lomonosov Moscow State University Program of Development. F.A., H.N., and K.I. thank Japan Society for the Promotion of Science (Project No. JPJSBP120214814), JSPS KAKENHI (JP22K14594, JP21H01801), JST CREST (JPMJCR17N1, JPMJCR23O1), and JST SICORP EIG CONCERT-Japan (JPMJSC22C3) for the financial support of the synthesis of the material used in this work. H.N. was supported by a RIKEN Special Postdoctoral Researchers (SPDR) fellowship.

- [1] R. J. Mandle, *Soft Matter* **18**, 5014 (2022).
- [2] A. G. Vanakaras and D. J. Photinos, *Mol. Cryst. Liq. Cryst.* **395**, 213 (2003).
- [3] H. Takezoe, *Ferroelectrics* **468**, 1 (2014).
- [4] H. Takezoe, *Mol. Cryst. Liq. Cryst.* **646**, 46 (2017).
- [5] F. Vita, F. C. Adamo, and O. Francescangeli, *J. Mol. Liq.* **267**, 564 (2018).
- [6] O. Francescangeli and E. T. Samulski, *Soft Matter* **6**, 2413 (2010).
- [7] A. V. Emelyanenko and M. A. Osipov, *Liq. Cryst.* **26**, 187 (1999).
- [8] E. Gorecka, D. Pocięcha, J. Mieczkowski, J. Matraszek, D. Guillon, and B. Donnio, *J. Am. Chem. Soc.* **126**, 15946 (2004).
- [9] C. F. C. Fitie, W. S. C. Roelofs, M. Kemerink, and R. P. Sijbesma, *J. Am. Chem. Soc.* **132**, 6892 (2010).
- [10] D. Miyajima, F. Araoka, H. Takezoe, J. Kim, K. Kato, M. Takata, and T. Aida, *Science* **336**, 209 (2012).
- [11] V. Novotna, M. Glogarova, V. Hamplova, and M. Kaspar, *J. Chem. Phys.* **115**, 9036 (2001).
- [12] D. Catalano, V. Domenici, A. Marini, C. A. Veracini, A. Bubnov, and M. Glogarova, *J. Phys. Chem. B* **110**, 16459 (2006).
- [13] A. Bubnov, V. Novotna, V. Hamplova, M. Kaspar, and M. Glogarova, *J. Mol. Struct.* **892**, 151 (2008).
- [14] Y. Na, Y. Naruse, N. Fukuda, H. Orihara, A. Fajar, V. Hamplova, M. Kaspar, and M. Glogarova, *Ferroelectrics* **364**, 13 (2008).
- [15] A. V. Emelyanenko, *Crystals* **9**, 583 (2019).
- [16] H. Nishikawa, K. Shiroshita, H. Higuchi, Y. Okumura, Y. Haseba, S. Yamamoto, K. Sago, and H. Kikuchi, *Adv. Mater.* **29**, 1702354 (2017).
- [17] R. J. Mandle, S. J. Cowling, and J. W. Goodby, *Chem. Eur. J.* **23**, 14554 (2017).
- [18] R. J. Mandle, S. J. Cowling, and J. W. Goodby, *Phys. Chem. Chem. Phys.* **19**, 11429 (2017).
- [19] A. Mertelj, L. Cmok, N. Sebastian, R. J. Mandle, R. R. Parker, A. C. Whitwood, J. W. Goodby, and M. Copic, *Phys. Rev. X* **8**, 041025 (2018).
- [20] R. J. Mandle and A. Mertelj, *Phys. Chem. Chem. Phys.* **21**, 18769 (2019).
- [21] S. Dhakal and J. V. Selinger, *Phys. Rev. E* **81**, 031704 (2010).
- [22] R. J. Mandle, N. Sebastian, J. Martinez-Perdiguero, and A. Mertelj, *Nat. Commun.* **12**, 4962 (2021).
- [23] R. J. Mandle, S. J. Cowling, and J. W. Goodby, *Liq. Cryst.* **48**, 1780 (2021).
- [24] E. Cruickshank, R. Walker, J. M. D. Storey, and C. T. Imrie, *RSC Adv.* **12**, 29482 (2022).
- [25] J. Li, Z. Wang, M. Deng, Y. Zhu, X. Zhang, R. Xia, Y. Song, Y. Hisai, S. Aya, and M. Huang, *Giant* **11**, 100109 (2022).
- [26] R. J. Mandle, *Liq. Cryst.* **49**, 2019 (2022).
- [27] X. Chen, V. Martinez, E. Korblova, G. Freychet, M. Zhernenkov, M. A. Glaser, C. Wang, C. Zhu, L. Radzihovsky, J. E. Maclennan, D. M. Walba, and N. A. Clark, *Proc. Natl. Acad. Sci. (USA)* **120**, e2217150120 (2023).
- [28] S. Brown, E. Cruickshank, J. M. D. Storey, C. T. Imrie, D. Pocięcha, M. Majewska, A. Makal, and E. Gorecka, *ChemPhysChem* **22**, 1 (2021).
- [29] J. Li, H. Nishikawa, J. Kougo, J. Zhou, S. Dai, W. Tang, X. Zhao, Y. Hisai, M. Huang, and S. Aya, *Sci. Adv.* **7**, eabf5047 (2021).
- [30] X. Chen, E. Korblova, D. Dong, X. Wei, R. Shao, L. Radzihovsky, M. A. Glaser, J. E. Maclennan, D. Bedrov, D. M. Walba, and N. A. Clark, *Proc. Natl. Acad. Sci. (USA)* **117**, 14021 (2020).
- [31] N. Sebastian, M. Copic, and A. Mertelj, *Phys. Rev. E* **106**, 021001 (2022).
- [32] J. Ortega, C. L. Folcia, and J. Etxebarria, *Liq. Cryst.* **49**, 2128 (2022).
- [33] H. Nishikawa and F. Araoka, *Adv. Mater.* **33**, 2101305 (2021).
- [34] X. Zhao, J. Zhou, J. Li, J. Kougo, Z. Wan, M. Huang, and S. Aya, *Proc. Natl. Acad. Sci. (USA)* **118**, e2111101118 (2021).
- [35] A. V. Emelyanenko, V. Yu. Rudyak, S. A. Shvetsov, F. Araoka, H. Nishikawa, and K. Ishikawa, *Phys. Rev. E* **105**, 064701 (2022).
- [36] M. P. Rosseto and J. V. Selinger, *Phys. Rev. E* **101**, 052707 (2020).
- [37] J. V. Selinger, *Annu. Rev. Condens. Matter Phys.* **13**, 49 (2022).
- [38] N. Sebastian, L. Cmok, R. J. Mandle, M. R. de la Fuente, I. Drevensek Olenik, M. Copic, and A. Mertelj, *Phys. Rev. Lett.* **124**, 037801 (2020).
- [39] A. Erkoreka, A. Mertelj, M. Huang, S. Aya, N. Sebastian, and J. Martinez-Perdiguero, *J. Chem. Phys.* **159**, 184502 (2023).
- [40] N. Sebastian, M. Lovsin, B. Berteloot, N. Osterman, A. Petelin, R. J. Mandle, S. Aya, M. Huang, I. Drevensek-Olenik, K. Neyts, and A. Mertelj, *Nat. Commun.* **14**, 3029 (2023).
- [41] R. Barboza, S. Marni, F. Ciciulla, F. A. Mir, G. Nava, F. Caimi, A. Zaltron, N. A. Clark, T. Bellini, and L. Lucchetti, *Proc. Natl. Acad. Sci. (USA)* **119**, e2207858119 (2022).
- [42] M. T. Mathe, B. Farkas, L. Peter, A. Buka, A. Jakli, and P. Salamon, *Sci. Rep.* **13**, 6981 (2023).
- [43] C. L. Folcia, J. Ortega, R. Vidal, T. Sierra, and J. Etxebarria, *Liq. Cryst.* **49**, 899 (2022).
- [44] K. Perera, R. Saha, P. Nepal, R. Dharmarathna, M. S. Hossain, M. Mostafa, A. Adaka, R. Waroquet, R. J. Twieg, and A. Jakli, *Soft Matter* **19**, 347 (2023).
- [45] A. Sterle, L. Cmok, N. Sebastian, A. Mertelj, Y. Kong, X. Zhang, and I. Drevensek-Olenik, *Opt. Mater. Express* **13**, 282 (2023).
- [46] S. Marni, G. Nava, R. Barboza, T. G. Bellini, and L. Lucchetti, *Adv. Mater.* **35**, 2212067 (2023).
- [47] J. Yang, Y. Zou, W. Tang, J. Li, M. Huang, and S. Aya, *Nat. Commun.* **13**, 7806 (2022).
- [48] F. Caimi, G. Nava, S. Fuschetto, L. Lucchetti, P. Paie, R. Osellame, X. Chen, N. A. Clark, M. A. Glaser, and T. Bellini, *Nat. Phys.* **19**, 1658 (2023).
- [49] R. Saha, P. Nepal, C. Feng, M. S. Hossein, J. T. Gleeson, S. Sprunt, R. J. Twieg, and A. Jakli, *Liq. Cryst.* **49**, 1784 (2022).
- [50] A. V. Emelyanenko, E. S. Filimonova, and A. R. Khokhlov, *Phys. Rev. E* **103**, 022709 (2021).
- [51] A. V. Emelyanenko and A. R. Khokhlov, *J. Chem. Phys.* **142**, 204905 (2015).
- [52] See Supplemental Material at <http://link.aps.org/supplemental/10.1103/PhysRevE.109.014701> for additional videos.
- [53] N. Sebastian, R. J. Mandle, A. Petelin, A. Eremin, and A. Mertelj, *Liq. Cryst.* **48**, 2055 (2021).
- [54] Yu. Garbovskiy, A. V. Emelyanenko, and A. Glushchenko, *Nanoscale* **12**, 16438 (2020).
- [55] A. V. Emelyanenko, *Phys. Rev. E* **82**, 031710 (2010).
- [56] A. V. Emelyanenko and M. A. Osipov, *Ferroelectrics* **309**, 13 (2004).
- [57] V. Yu. Rudyak, A. V. Emelyanenko, and V. A. Loiko, *Phys. Rev. E* **88**, 052501 (2013).